Research Square

Preprints are preliminary reports that have not undergone peer review.
They should not be considered conclusive, used to inform clinical practice,
or referenced by the media as validated information.

Experimental and Numerical Investigation of Microstructural Evolution, Mechanical Behaviour and Fracture Characteristics of Autogenous GTAW-Welded Duplex Stainless Steel 2205

Sujeet Kumar
Bonam Venkata Chalamayya College of Engineering
Aimin Li
Xi'an University of Technology
Saurav Mallik
sauravmtech2@gmail.com

The University of Texas at El Paso https://orcid.org/0000-0003-4107-6784

Research Article

Keywords: Duplex stainless steel 2205, GTAW, microstructural evolution, SEM–EDS, Microhardness, tensile behaviour, ductile fracture, von Mises stress

Posted Date: November 20th, 2026

DOI: https://doi.org/10.21203/rs.3.rs-11644318/v1

License: This work is licensed under a Creative Commons Attribution 4.0 International License.
Read Full License

Experimental and Numerical Investigation of Microstructural Evolution, Mechanical Behaviour and Fracture Characteristics of Autogenous GTAW-Welded Duplex Stainless Steel 2205

Sujeet Kumar[1,*], Aimin Li[2], Saurav Mallik[3,4,*]

[1]Department of Mechanical Engineering, Bonam Venkata Chalamayya Engineering College, Odalarevu, 533210, Andhra Pradesh, India; sujeet731@gmail.com

[2]School of Computer Science and Engineering, Xi'an University of Technology, Xi'an, 710048, Shaanxi, China; liaiminmail@gmail.com, Aimin.Li@xaut.edu.cn

[3]Department of Environmental Health, Harvard T H Chan School of Public Health, Boston, MA 02115, USA; smallik@hsph.harvard.edu

[4]Department of Biological Sciences, University of Texas at El Paso, El Paso, TX 79968, USA; sauravmtech2@gmail.com; smallik@utep.edu

***Correspondence:** Sujeet Kumar (sujeet731@gmail.com); Saurav Mallik (sauravmtech2@gmail.com; smallik@utep.edu)

Abstract

This research paper examines microstructure evolution, mechanical properties and fracture behavior of 2 mm thin Duplex Stainless Steels (DSS 2205) plate joint through the process of Autogenous Gas Tungsten Arc Welding (GTAW). Microstructural analysis of base metal (BM), heat affected zone (HAZ) and weld zone (WZ) is done using optical microscopy and quantitative Phase Analysis. The ferrite percentages are 48.4% in BM, 50.2% in HAZ to 51.7% in WZ while the austenite percentages reduced from 51.6% in BM to 49.8% in HAZ and 48.3% in WZ respectively. Microchemical composition analysis is done using scanning electron microscope-energy dispersive spectroscopy and found that there is compositional segregation in the two microstructural phases. Microhardness of the BM, HAZ and WZ are 221.25 HV, 231.67 HV and 239 HV, respectively, indicating an 8.0% increase in WZ hardness relative to the BM. Tensile testing on the BM and the welded specimens provided ultimate tensile

strengths of 766 MPa and 762 MPa, indicating 99.48% retention of tensile strength. Analysis of the stress-strain plot indicates that the area under the curve up to the UTS is decreased by 13.24% and the entire area over the range of data is decreased by 3.42% in the welded specimen. SEM fractography indicated predominance of ductile fracture features including fine and large dimples, micro voids and interdimple ligaments, which indicate microvoid nucleation, growth and coalescence of the fractured surfaces. Abaqus/Explicit FEM provided maximum von Mises stress values of 277.1 MPa and 264.8 MPa for the BM and welded samples, respectively, which is a decrease of 4.44% in the maximum numerical contour.

Keywords: *Duplex stainless steel 2205; GTAW; microstructural evolution; SEM–EDS; Microhardness; tensile behaviour; ductile fracture; von Mises stress.*

Introduction

Duplex Stainless Steel (DSS) 2205 is a critical engineering material for use in structures, marine applications, chemical processing plants, offshore and energy industries due to its high strength and corrosion resistance[1, 2]. These properties are obtained from a dual-phase microstructure comprising mainly of ferrite (δ) and austenite (γ) in balanced proportions. The element chromium enhances the formation of a passive oxide film, molybdenum increases resistance to pitting and crevice corrosion while nitrogen provides strength, pitting resistance, and stabilization of austenite. The ferritic phase is known to provide strength and chloride stress corrosion cracking resistance while the austenitic phase offers ductility and toughness[3, 4]. The synergy of these phases gives the duplex 2205 alloy a better combination of mechanical and corrosion properties than many conventional austenitic stainless steels[5]. These properties highly depend on the phase balance, grain structure, chemical composition and thermal history of the material. The welding process alters these microstructural properties, thus making the evaluation of welded joint properties a critical engineering problems[6, 7].

The gas tungsten arc welding (GTAW), or tungsten inert gas (TIG) welding method is widely applied to weld stainless steels requiring stable heat input and quality weld. In GTAW, an electric arc is created between a non-consumable tungsten electrode and a workpiece under a protection of an inert shielding gas. This technique is suitable for thin plates due to precise control of the welding arc and capability of making narrow weld with low levels of spattering[8, 9]. The thermal cycle of welding provides high temperature gradients and local heating and cooling rates affecting solidification, phase transformation, residual stresses, and HAZ

creation. It is especially important when it comes to welding of duplex stainless steels as in this case the amount of ferrite–austenite depends on the maximum reached temperature, cooling rate, chemical composition, and the presence of nucleation sites for austenite[10, 11]. Ferrite over formation, big grain size or undesirable distribution of secondary phases might decrease toughness and corrosion resistance[12, 13]. The controlling welding parameters and studying the resulted microstructure is important for evaluating mechanical properties of DSS 2205 welded joints. The autogenous GTA welding there is no filler metal addition, presents an effective method in analyzing the impact of the parent material and the heat-affected zone (HAZ) thermal cycle in the absence of the additional component introduced by the filler metal wire. The weld material is obtained mostly by melting of the base metal. It is easier to interpret the joint between the base material, fusion zone (FZ) solidification, and its mechanical behavior. But then again, because there is no filler metal to add, there is no possibility of controlling the composition in such a way that it aids in making austenite[14, 15]. The mechanical and microstructure behavior is not known from the characteristics of the base material, but only through experimental study. It becomes very important in thin DSS 2205 sheets since a small change in energy input or travel speed results in changes to the thermal cycle in a considerable portion of the sheet thickness. The relatively thin plate makes it important to examine the interaction between welding energy, cooling conditions, weld geometry, and local mechanical behaviour. Published research on duplex stainless steel weldments has shown that both insufficient and excessive thermal input can produce undesirable microstructural conditions. Rapid cooling is restrict austenite reformation and promote ferrite-rich structures, whereas prolonged exposure to elevated temperatures is encourage grain coarsening and the formation of deleterious intermetallic phases, including sigma (σ) and chi (χ), under suitable conditions[16, 17]. Microstructural characterization is necessary for understanding the mechanical behavior of the weld material. The base metal has a typical ferrite–austenite microstructure formed during the manufacturing process of the plate. In contrast, the HAZ undergoes a heating cycle without melting. Near the fusion line, the high peak temperature can dissolve the austenite and cause ferrite grains to grow, followed by the formation of new austenite upon cooling[18]. The weld metal has gone through the process of melting and solidification, normally starting with ferritic solidification and later forming austenite. Because of the thermal cycle of the weld, austenite forms either grain-boundary, Widmanstätten, or intragranular structures[19]. Purpose of the micrographs is to differentiate the three regions (BM, HAZ and WZ) qualitatively. The volumes of the ferrite and austenite should not be given unless the proper quantitative image analysis is done. Microhardness

testing offers another technique to analyze the mechanical behavior in the welded joint. The hardness profile obtained can be related to the changes in the morphology of ferrite-austenite, grain size, and geometry of the weld region. The increase in the local hardness is be due to phase morphology, grain size, or any other mechanical change, but the hardness value cannot determine which phase it is and the reason for mechanical change[20, 21]. Hence, the hardness values are analyzed along with the micrographs and tensile tests.

Tensile test is a basic testing procedure for analyzing the strength and ductility of metallic materials subjected to uniaxial stress conditions. Yield or proof strength, ultimate tensile strength (UTS), elongation, and reduction in area could be determined by standardized tensile tests depending on the specimen dimensions and equipment used. In this current experiment, base metal samples and transverse weld samples are used to assess the effect of GTAW joining process on the mechanical behaviour of DSS 2205. Tensile behaviour of the weld sample shows the combined effects of base metal, HAZ and WZ as several metallurgically different regions have been observed in the gauge section of the sample[21, 22]. The Finite Element Analysis (FEA) offers a supplementary technique for investigating stress redistribution and deformation in welded tensile samples. Tensile testing experiment provides the overall behavior of the sample but cannot provide the internal stress and strain field directly. FEA allows the spatial distribution of stress, displacement, and plastic deformation to be estimated for a specified loading and boundary condition[23]. Abaqus/Standard is appropriate for modeling quasi-static tensile deformation using the elastic–plastic constitutive model. In the standard isotropic plasticity model, the elastic behavior of the material is described using the Young's modulus and Poisson's ratio, and the plastic behavior is described using the stress-plastic strain model[24, 25]. True stress and true plastic strain for the material can be calculated using the engineering stress–strain data in the uniform-deformation regime and can be inputted in the model. Reaction force and displacement of the gauge section can then be used to construct the load-displacement curve and the engineering stress-strain curve of the sample[26, 27]. In the case of a sample, the numerical description of the welding region is especially crucial. A homogeneous model can mimic the overall tensile behavior, provided that it is calibrated correctly; however, it cannot specifically represent the behavior of the base metal, HAZ, and weld metal. A spatially segmented model provides a more sophisticated description in that it assigns different constitutive behaviours to each of these zones. According to Çelik et al. joining of UNS S31803 duplex stainless steel pipes through a combination of GTAW and SMAW techniques produced joints with high strength and hardness properties that complied

with specifications. Through control of the heat input and interpass temperature during the multiple passes, it is possible to avoid brittle sigma phase formation[28]. Touileb et al. analyzed the welding process between 2205 duplex and 316L austenitic stainless steels through dissimilar ATIG welding utilizing an optimal flux mixture to attain single-pass full penetration without the need for edge preparation. It is able to greatly enhance the tensile strength with a heat-affected zone that is 2.6 times smaller than traditional TIG welding[29]. Gao et al. used finite element modeling together with microstructure experiments in order to study the deformation behavior of TIG weld joints in 2205 duplex stainless steel. It is established that macroscopic strain distribution is strongly affected by local phase changes and morphological transformations[30]. Verma and Taiwade reviewed extensively the effects of different welding techniques and process parameters on the microstructure, strength properties, and corrosion resistance of the weldments of duplex stainless steel. The authors stressed that achieving the optimum balance between austenite and ferrite is necessary to avoid microstructural damage arising from undesirable intermetallic phases and ferrite growth in the heat-affected zone [31]. The development of such a model should rely on reliable zone-specific properties or reasonable approximations. An arbitrary assignment of different yield strengths and plasticity curves for each zone could lead to the misrepresentation of the stress and strain field. For the current work, the Abaqus model is to be created based on experimentally validated material properties, the level of which will be defined by the available information. Numerical stability will be checked through mesh refinement around the weld and HAZ and mesh convergence analysis. The obtained von Mises stress and equivalent plastic strain distribution will allow defining the localization regions and interpreting them in light of the experiment. Objectives of this study are to investigate the microstructural development, phases distribution, and mechanical behavior of 2 mm thick DSS 2205 plates joined by the autogenous gas tungsten arc welding process. The emphasis was on the quantitative assessment of phases, SEM-EDS characterization, microhardness testing, tensile behavior, and fractographic analysis. Also, numerical investigations have been carried out in order to assess the von Mises stress distribution in the base metal as well as in the welded joint using the finite element modeling technique in Abaqus/Explicit software. Correlations have been observed between welding-induced microstructure and mechanical behavior of DSS 2205.

2. Materials and Experimental Methodology

2.1 Material and Welding Procedure

For the scope of this research, 2 mm thick plates of DSS 2205 duplex stainless steel are selected as the base material. The Chemical composition and Mechanical-thermal properties of DSS 2205 are given in **Table 1** and **Table 2,** respectively. They are joined in autogenous GTAW, where no filler metal is added. Prior to the joining, the plate surfaces are cleaned from contaminants and the joint edge is prepared for uniformity of alignment and welding conditions. The welding is done at a current of 80 A and 12 V arc voltage with a travel speed of 100 mm/min, an argon shield is applied at the rate of 15 L/min for protection of the melt pool from atmosphere. With regard to electrical power, the nominal value equals 960 W or 576 J/mm per unit length of the weld seam, but it should not be mistaken for heat input into the material. After welding, the plates are allowed to cool down in laboratory conditions. From them, the test specimens are machined for tensile, microhardness and metallography, whereas some specimens from unwelded stock are kept as reference. All necessary data regarding material state, geometrical and technical characteristics of the weld seam have been documented to serve as reliable background for modelling and experimental studies. The research methodology of the research work is shown in **Figure 1**. The GTAW machine Setup schematic digram is shown in **Figure 2**.

Table 1: Chemical composition of DSS 2205 (UNS S32205)

Symbol	**Cr**	**Ni**	**Mo**	**N**	**C**	**Mn**	**Si**	**P**	**S**	**Fe**
Nominal (%)	22.5	5.4	3.1	0.19	0.021	1.01	0.51	0.016	0.005	Balance

Table 2: Mechanical and Thermal Properties of DSS 2205 [30]

Property	**Typical Value**
Charpy V-Notch Impact Energy (Room Temp) (J)	85
Modulus of Elasticity (Young's Modulus)(GPa)	200
Density(g/cm3)	7.80
Melting Range(°C)	1440

Linear Thermal Expansion Coefficient (μm/m·°C)	13.7×10^{-6}
Thermal Conductivity (at 20 °C) (W/(m·K)	19.0
Specific Heat Capacity (at 20 °C) (J/(kg·K))	500
Electrical Resistivity(μΩ·m)	0.80

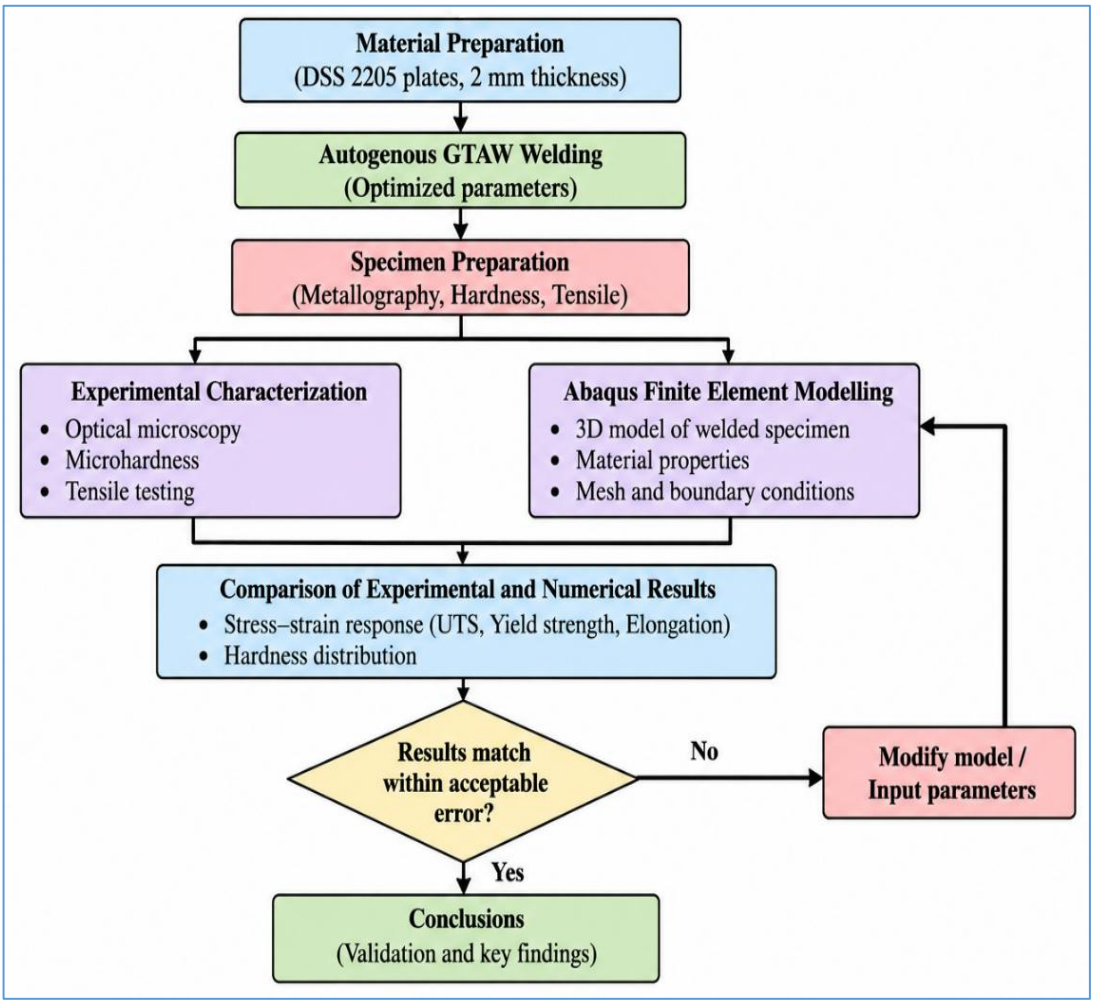

Figure 1: Research Methodology.

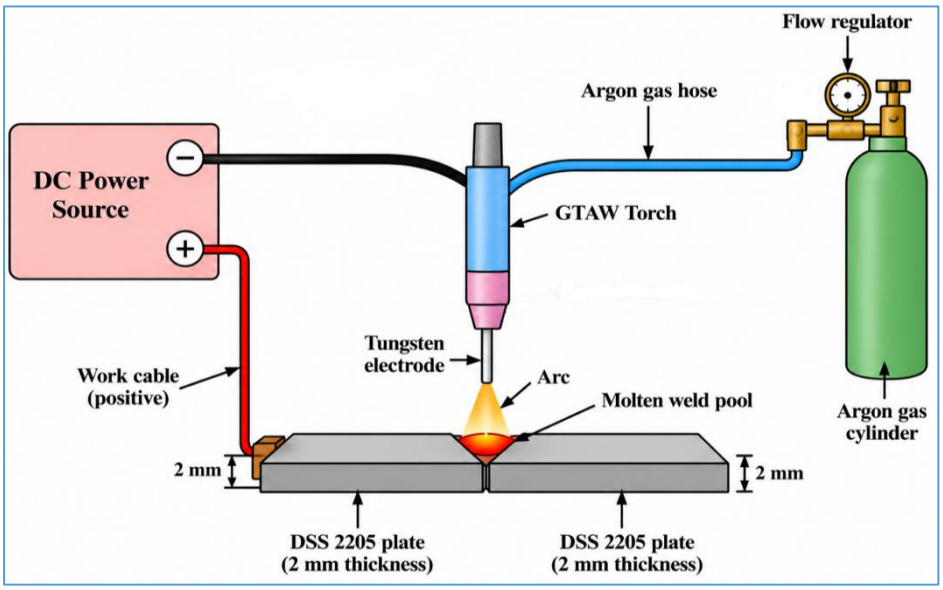

Figure 2: GTAW Setup for experiment.

2.2 Microstructural Characterization and Microhardness

In order to determine the impact of GTAW thermal cycle on the grain structure and phases morphology of the DSS 2205, a microstructural analysis is conducted. Metallographic specimens are cut at the right angles to the weld in order to observe the WZ, HAZ and base metal. After that, samples are subjected to grinding and polishing with proper abrasives for optical evaluation. Then welded joint samples are etched using the proper etchant for duplex stainless steels. Beraha's reagent (20 mL HCl, 80 mL distilled water, and 1 g potassium metabisulfite). Microstructural analysis is performed with a Leica DM700 optical microscope. We use the appropriate magnification for optical micrographs to study features like ferrite-austenite structure, fusion boundaries and other welding characteristics. Hardness of the material is determined by performing a traverse which goes from one side of the base metal to another. We make Vickers indentations which are of the proper load and dwell time as per the specimen thickness and testing criteria. The microhardness tests are done via the Vickers hardness test technique which we apply a load of 500gf (HV0.5) for a duration of 15 seconds. We take hardness readings in the base metal, heat affected zone, and weld metal to see any hardness variations in the GTAW weld of DSS 2205 material.

2.3 Tensile Testing preparation

Tensile testing is used to study the mechanical properties of autogenous GTAW welded and unwelded DSS 2205. We made the samples to match the 2 mm plate and corresponding standard. The tests are performed per ASTM E8/E8M on 120 x 10 x 2 mm samples for length,

width and thickness respectively. We calibrated the machine and maintained room temperature at a constant value then we measured the original length, width and thickness to determine the cross sectional area. The machine records the elongation and load during the test. We then calculated the engineering strain from the extension and stress from the initial area. One out of the resulting curves we get the ultimate tensile strength, elongation and 0.2% proof stress. Also we note the peak load for use in the FEA results comparison. Fracture is determined which may have happened at the weld, HAZ or parent material. If we have enough samples the mean and standard deviation are calculated. In total these results are used to validate the constitutive material properties for Abaqus modeling.

2.4 Finite Element Modelling

Abaqus/Standard is a three-dimensional FEM tool is established for investigating the tensile behaviour of the welded joint in the quasi-static loading condition. The dimensions of the weld position, gauge section, etc., are determined as per their experimentally measured values. Based on the available information, the model is discretised into the regions of WM, HAZ and BM as shown in **Figure 3**. The material is characterised using the elastic-plastic constitutive law, wherein the elastic properties including Young's modulus and Poisson's ratio are taken from the reliable source, and the plastic properties from the tensile curves. The engineering stress-strain data are first converted to the true stress-plastic strain form and then applied. Spatial variation in deformation is considered in terms of mesh refinement of the solid part in the region around the weld and HAZ. Appropriate boundary conditions in the form of the experimentally performed one are prescribed in a static general analysis step, considering geometric non-linearity where necessary. Finally, the output data of interest including the von Mises stress, reaction force, equivalent plastic strain, and other outputs are extracted from the simulation results. Convergence study is done through the load response comparison of successively refined meshes. For fracture initiation and analysis Mathematical representations of Johnson–Cook (J–C) material model is used given in **Table 3**.

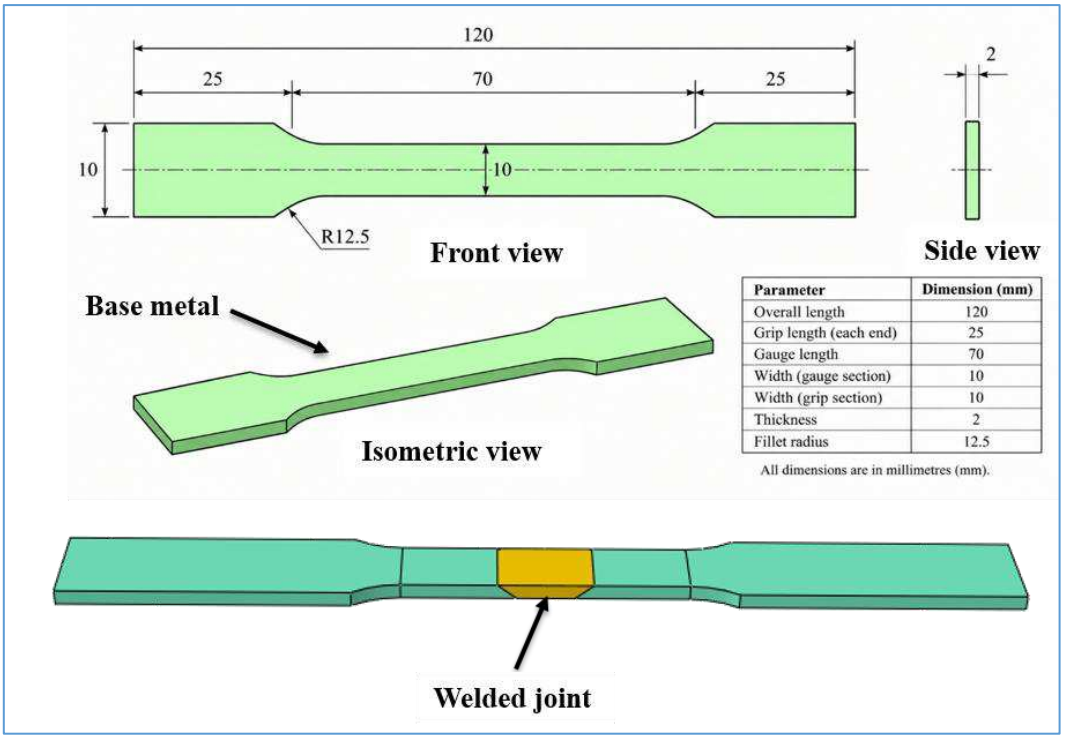

Figure 3: *Tensile test model.*

Table 3: Mathematical reprentations of Johnson–Cook (J–C) material model

Johnson–Cook model represents the von Mises flow stress	$\bar{\sigma} = [x + y(\bar{\varepsilon}^{ql})^n]\left[1 + Cln\left(\dot{\bar{\varepsilon}}^{ql}/\dot{\bar{\varepsilon}}_0^{ql}\right)\right]$ $[1 - T^{*m}]$	
Damage parameter (D)	$D = \Sigma\left(\Delta\,\bar{\varepsilon}^{ql}/\dot{\bar{\varepsilon}}_D^{ql}\right)$	
Equivalent plastic strain at the onset of damage	$\bar{\varepsilon}_D^{ql} = [\,P_1 + P_2\exp(-P_3\eta)][1 + P_4\ln(\dot{\bar{\varepsilon}}^{ql}/\dot{\bar{\varepsilon}}_0)][\,1 + P_5T^*]$	
Homologous temperature	$T^* = (T - T_{room})/(T_{melt} - T_{room})$	
Notation	Description	Unit/Value
$\bar{\sigma}$	Von Mises flow stress.	MPa
$\dot{\bar{\varepsilon}}^{ql}$	Equivalent plastic strain rate	2100
$\dot{\bar{\varepsilon}}^{ql}/\dot{\bar{\varepsilon}}_0^{ql}$	Normalized equivalent plastic strain rate	------
T^*	Homologous temperature.	Kelvin
	J-C parameters value	
A	J-C yield strength	593(MPa)

B	J-C hardening coefficient	331(MPa)
n	J-C strain hardening exponent	0.33
C	J-C strain rate constant	0.015
m	J-C softening exponent	0.81
T_{melt}	Melting temperature	1352 (K)
η	$-p/\bar{\sigma}$ is the stress triaxiality defined as an average of three normal stress, p, to the von Misses stress $\bar{\sigma}$	
$\overline{\varepsilon_D}^{ql}$	Equivalent damage plastic strain in J-C model.	
P_1	J-C damage constant	0.05
P_2	J-C damage constant	0.05
P_3	J-C damage constant	2.12
P_4	J-C damage constant	0.0002
P_5	J-C damage constant	0.61

2.5 Experimental–Numerical Validation

To validate the numerical model, the tensile response as measured in the lab is put up against the predictions of an Abaqus finite element analysis. In processing both the experimental and simulated data, we made sure to apply uniform definitions for gauge length, initial cross-sectional area, and the engineering stress and strain. From the finite element output, reaction force and gauge-section displacement are taken to build a load–displacement curve and, in suitable cases, an engineering stress–strain curve. The ensuing comparison covered a range of features: the initial elastic and yield behaviour, maximum load, ultimate tensile strength and deformation. We also looked at the predicted von Mises stress and equivalent plastic strain to spot any areas of plastic deformation or stress concentration, interpreting these in the context of the weld geometry, optical micrographs, microhardness profile and where the fracture is recorded in the experiment. Any discrepancy in the key mechanical quantities is quantified by the % error from the experimental figures. Rather than relying on a single maximum-strength number, the degree of agreement between the two sets of results is judged on several metrics. Mesh convergence is checked on its own to be certain

the discretization is stable enough for the principal response. The constitutive model's limitations are factored in as well; since standard elastic–plastic modelling will not on its own predict material failure, zones with high plastic strain are viewed as likely sites of deformation localisation in the absence of a calibrated damage model. In this way, a systematic appraisal of the model's suitability for welded DSS 2205 is achieved.

3. Results and discussions

3.1 Microstructural analysis

Figure 4(a) shows the schematic welded joint, including the base metal, heat-affected zone (HAZ), and weld zone (WZ). DSS 2205 contains two main phases—ferrite and austenite—as shown in **Figure 4(b)**. In the base metal, a ferritic matrix surrounds austenite regions whose shapes vary with the processing conditions and the plate's rolling direction; **Figure 4(c)** shows elongated, rounded, and banded forms. The optical micrograph contains dark and bright areas, along with irregular phase boundaries and elongated features. Etching produces these contrasts, which correspond to the ferrite and austenite phases. Chromium and molybdenum promote ferrite formation and improve corrosion resistance, whereas nickel and nitrogen promote austenite formation. Duplex microstructure includes properties of ferrite and austenite, such as strength and toughness/ductility, respectively. Phase balance should be estimated quantitatively, not optically. The heat-affected zone undergoes the thermal cycle produced by GTAW but is not fully melted. At the same time, in DSS 2205, heating may dissolve austenite and favor ferrite formation at high peak temperatures. With further cooling, austenite may precipitate along the ferrite grain boundaries or inside the ferrite grains.This process is mostly a function of peak tempers, cool rate, plate thickness, and nitrogen. We see that the weld zone is made up of melted and recrystallized parent DSS 2205 material which does not include the filler metal. Solidification of duplex stainless steel is in the order of first formation of ferrite and then of austenite. Based on the thermal history the weld metal may consist of grain boundary austenite, Widmanstätten austenite (WA) and intragranular austenite. Grain boundary austinite (GBA) forms preferentially at the ferrite grain boundaries as a result of cooling. It appears as thin films or irregular bands which surround the ferrite grains in etched micrographs.

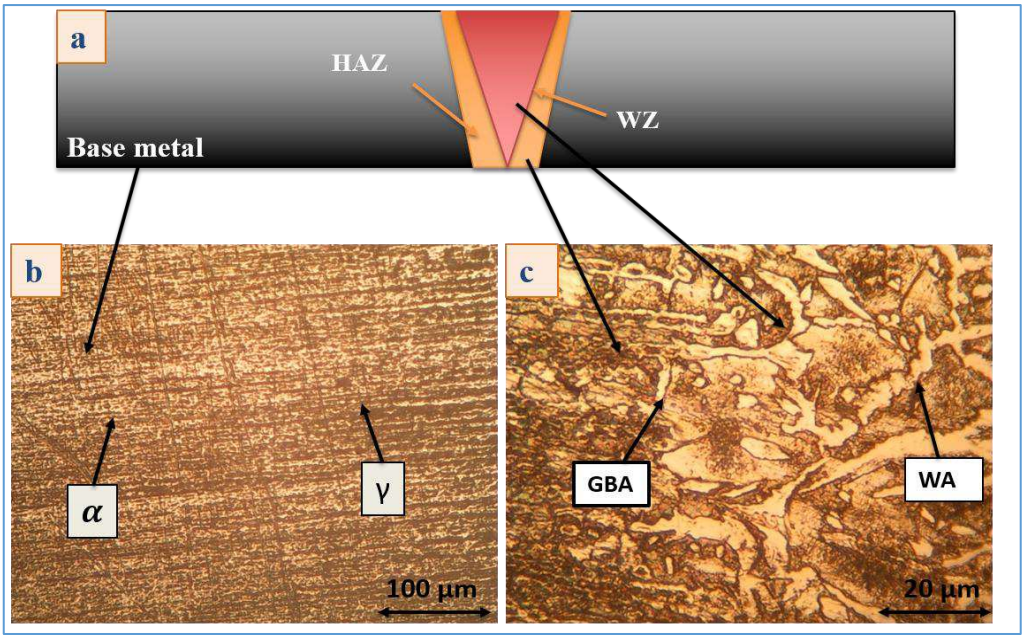

Figure 4: Microstructures of (a) Schematic representation of welded joint, (b) base metal and, (c) HAZ and WZ.

In the HAZ we see the reformation of austenite after high temp welding. In the WM GBA develops at the solidified ferrite grain boundaries. It is identified in the WM and HAZ of welded DSS 2205. WA is seen as elongated plates in the ferrite fields. Its morphology is a function of the welding thermal cycle, heat input and cooling rate. What we note is that the development of different microstructures of WZ and the base metal is a result of the appearance of WA. In the case of IGA it is present in the ferrite grains as fine particles, short plates, and isolated areas. The growth of IGA is a function of nucleation conditions and the time for transformation during cool down. Fast cool down which is to be expected in a weld environment does not support IGA growth because of limited diffusion and growth. Its morphology which in turn is different from grain boundary and Widmanstätten austenite. In welded DSS 2205 secondary austenite (γ2) is a result of reheating or to and from thermal cycles, mainly in multipass welding. In terms of corrosion behavior that is different from the primary austenite. In single pass autogenous GTAW secondary austenite formation is a little less due to reheating. The presence or absence of secondary austenite has to be determined through microstructural analysis. Also which in case of DSS 2205 we see sigma (σ) and chi (χ) intermetallics, chromium nitrides (Cr2N), chromium carbides, and secondary austenite (γ2) as some of the harmful secondary phases. These phases are a result of certain thermal conditions which arise during the processes of welding, cooling and reheating. The creation of such phases results in altering phase equilibrium, loss of toughness, and corrosion resistance because of the depletion of

chromium and other alloying elements. Fast cooling encourages chromium nitride formation, while heating promotes intermetallics formation. Such phases do not occur in DSS welded joints. The austenite and ferrite phase fractions in DSS 2205 base metal as well as welded joint is given in **Figure 5**.

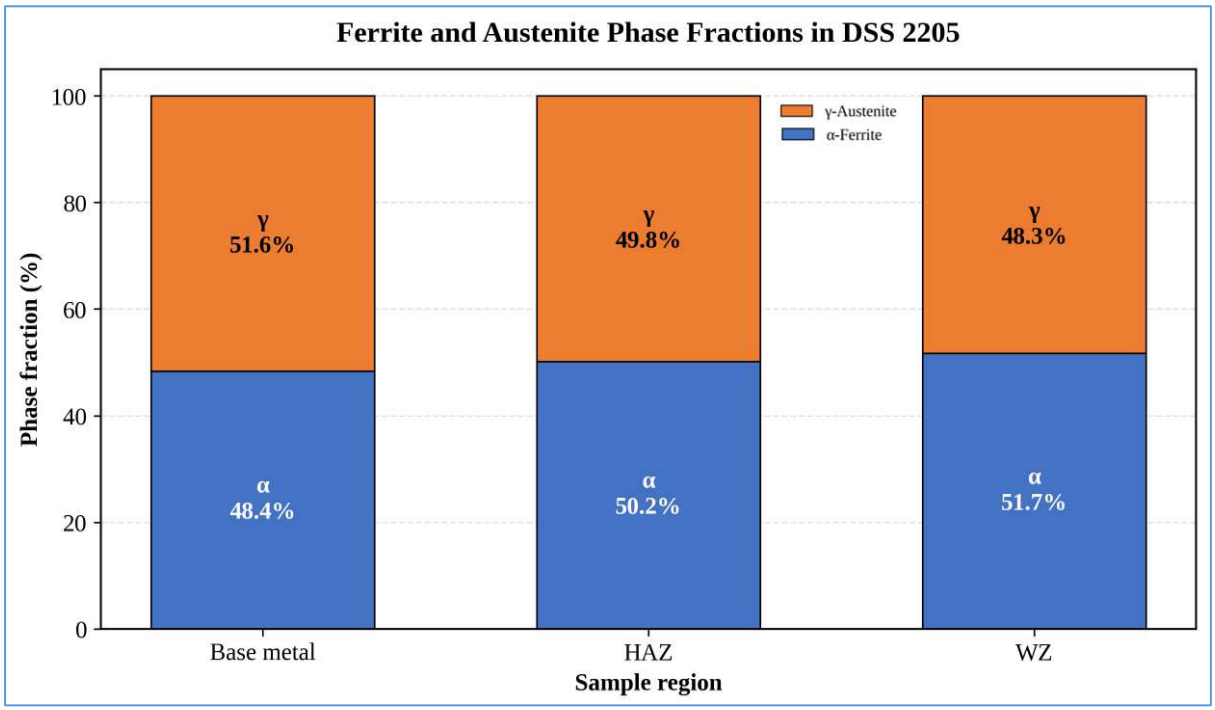

Figure 5: Austenite and ferrite phase fractions in DSS 2205.

3.2 Microhardness analysis

The average microhardness value of the base metal is 221.25 ± 2.75 HV, considering four indentation values varying from 218 to 224 HV. The HAZ demonstrated a greater microhardness value of 231.67 ± 1.53 HV, with indentation values ranging from 230 to 233 HV, which indicates a hardness increase of 4.7% as compared to the base metal given in **Table 4**. This increase in hardness is attributed to microstructural alterations produced by the welding process, such as changes in morphology of ferrite-austenite phases, structure of grains, and transformation behavior in heat treatments. The WZ had a greatest microhardness value of 239.00 7.07 HV which is a report of two indentations of 234 and 244 HV that represent an 8.0% increase in hardness as compared to the base metal as seen in **Figure 6**. Also we see that the large standard deviation in the fusion zone which is between the two measures reports more variation between the measurements, although the small sample size does not allow for any large scale conclusions. But we do see a trend of increasing hardness values from Base Metal to HAZ and FZ which in turn proves that the welding process affected the local material's resistance to indentation. For better assessment of the means and variability, we should perform

more indentations in all regions. The chromium content distribution reports that in general there is more Cr in ferrite than in austenite within the WZs. In Zone 1 can see 21.18 wt. % and 22.51 wt %. of Cr in austenite and ferrite respectively. In Zone 2 we see 22.15 and 23.58 wt %. in austenite and ferrite. Zone 3 reports 22.60 wt %. and 23.22 wt %. in austenite and ferrite. The greatest difference is in Zone 4 which has 26.74 wt. and 22.51 wt. of Cr in ferrite and austenite. This is the maximum value of Cr content. In Zone 5 can see 21.28 and 22.57 wt %. in austenite and ferrite respectively. Base metal has 22.49 and 21.99 wt %. of Cr in austenite and ferrite as shown in **Figure 8(a)**. The base metal's trend has changed, indicating a local variation in the composition of particular phases. This is to be read in light of the measurement uncertainty and the technique of analysis. Molybdenum levels are quite disparate from one phase to the other. In Zone 1 the molybdenum content is 3.33 wt.% for the austenite and 3.19 wt.% in the ferrite. For zone 2 the figure in austenite is down to 2.29 wt.% while it is up to 5.67 wt.% in the ferrite. As for Zone 3, there is 3.89 wt.% molybdenum in the austenite and 5.23 wt.% in the ferrite. Zone 4 is of a like concentration at 3.73 and 3.85 wt.%. The molybdenum content in the austenite of Zone 5 is the highest at 4.26 wt.%, as against 3.54 wt.% in the ferrite. As for the base metal, **Figure 8(b)** shows molybdenum to be 3.52 wt.% in the austenite and 5.58 wt.% in the ferrite. While these discrepancies point to some local heterogeneity in the chemical or phase composition, they do not substantiate the existence of secondary phases. In Zone 1 the Ni content is 6.50 and 5.77 wt.% for austenite and ferrite. In Zone 2, both the phases have comparable Ni content of 6.21 and 6.24 wt.%. Zone 3 has Ni content of 7.52 and 5.26 wt.% in austenite and ferrite, respectively. Zone 4 shows Ni content of 7.80 and 5.65 wt.% in austenite and ferrite, while Zone 5 has Ni content of 6.80 and 5.08 wt.%. The base metal has the highest Ni content of 8.29 wt.% in austenite, while ferrite has the Ni content of 5.17 wt.% shown in the **Figure 8(c)**.

Table 4: Descriptive statistics for Vickers microhardness measurements across the welded DSS 2205 joint

Location	Individual readings (HV)	n	Mean (HV)	SD (HV)	Minimum (HV)	Maximum (HV)
Base metal	218, 220, 224, 223	4	221.25	2.75	218	224
HAZ	230, 232, 233	3	231.67	1.53	230	233
Fusion zone (FZ)	234, 244	2	239.00	7.07	234	244

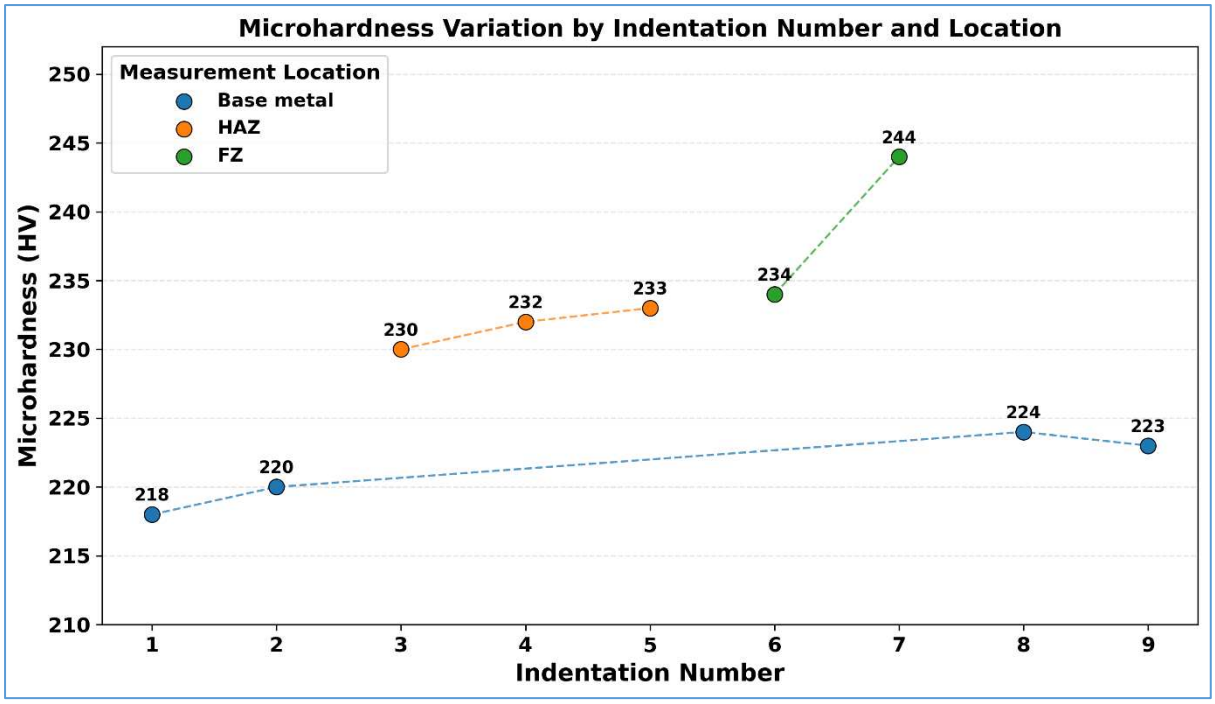

Figure 6: Microhardness variation with indentation number and location.

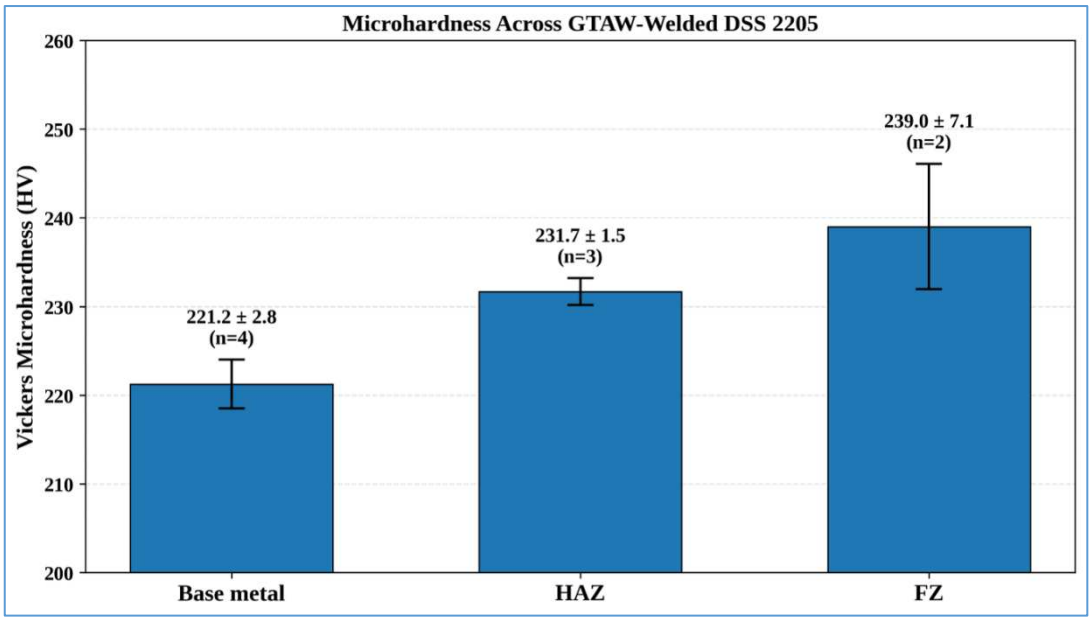

Figure 7: Microhardness across GTAW welded joint.

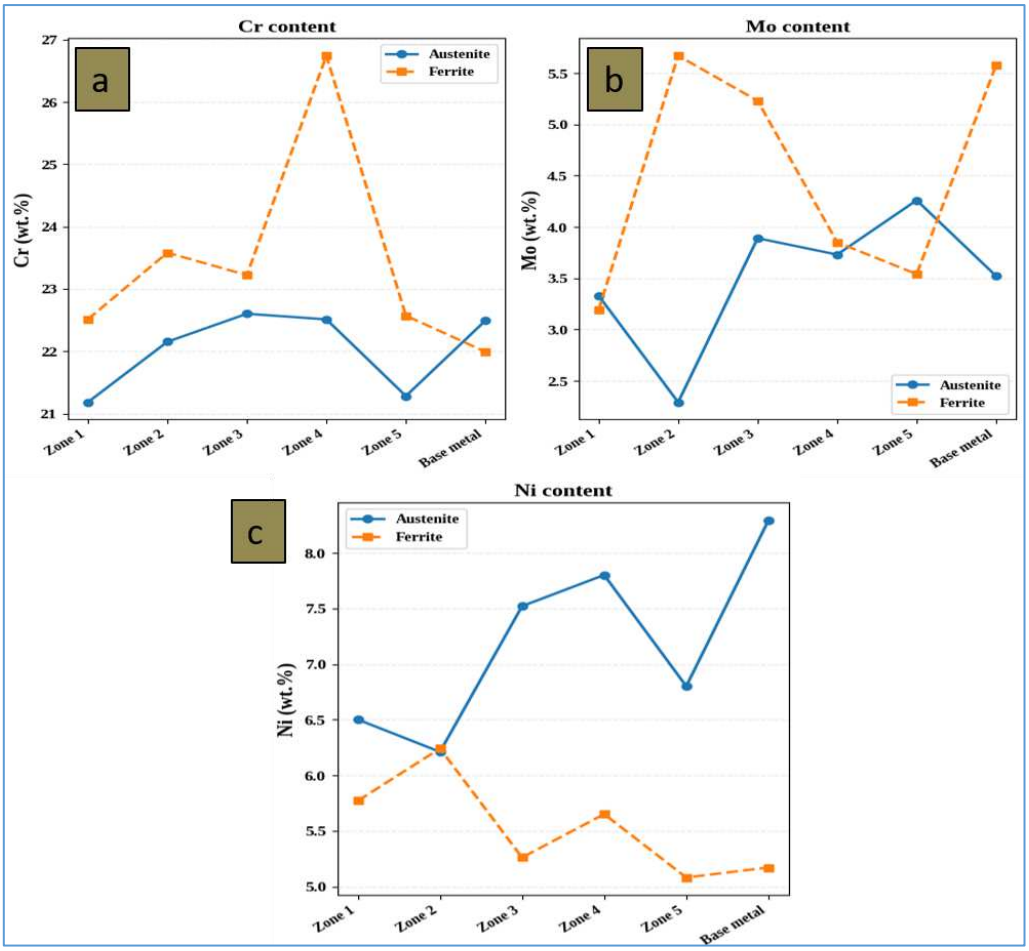

Figure 8: Comparative variation in the elemental composition across different weld regions, (a) Cr content, (b) Mo content, and (c) Ni content (wt.%).

3.3 Tensile test analysis

The base metal had the maximum engineering stress of 766 MPa at the engineering strain of 26.0%, while the welded joint had the maximum engineering stress of 762 MPa at 24.6% strain. With a 4 MPa gap in maximum tensile strength between the two specimens, the welded joint is 0.52% lower than the base metal. With another way, the joint has 99.48% of the UTS of the base metal, an indication of good tensile-strength retention following the autogenous GTAW welding. The stress-strain behavior of the base metal shows that stress will rise with strain until it reaches a maximum and then the engineering stress falls off in the post-peak deformation region as shown in **Figure 9**. The welded joint behaves excellent, except its maximum stress comes at a little lower strain level. The deformation of the base metal's stress is 589 MPa for a final strain of 29.7%, as compare to 620 MPa at 30.0% for the welded joint. The drop in engineering stress past the peak can be put down to necking and localized plastic

deformation once the highest loading is put on the material. The elastic phase is evident in the early part of the curve with stress increasing in proportion to the strain before the onset of plastic deformation. From the slope of the linear elastic regime one can derive Young's modulus and the 0.2% offset method will give the proof stress. There is an odd plateau at 10.2 MPa in some of the initial base-metal data over a portion of the strain interval. Strain at maximum stress point of base metal is 1.4 % larger compared to that of the welded joint, indicating different strain behaviors of these materials. The reason can lie in microstructure and HAZs due to the effect of welding of DSS 2205. Under autogenous GTAW the welding zone experiences melting and solidification while HAZ is heated and subsequently cooled. This thermal history can affect the properties of this zone and ferrite - austenite microstructure in this zone which would influence the tensile properties of the specimen. The ultimate tensile strength values obtained are not very different from each other meaning that the tensile strength of the welding zone is equal to the strength of the base material because the process parameters are perfect. However, one cannot use tensile strength as an indicator of whether any flaws exist in the process and also of how failure occurs. One also cannot use the strain values of 29.7% and 30.0% to represent elongation at fracture. It is important to identify whether the fracture originated from the base metal, HAZ or the weld metal. A microscopic examination of the fracture plane should provide some more information in respect of ductile dimpling, cleavage planes, as well as initiation and propagation of cracks. A few tensile tests would be useful to obtain average and standard deviation values, as well as ensure consistency in results. Ultimately, it can be stated that the autogenous GTAW weldment in the DSS 2205 steel achieved an engineering stress of up to 762 MPa. The base metal had a strength up to 766 MPa or 99.48 % of its tensile strength.

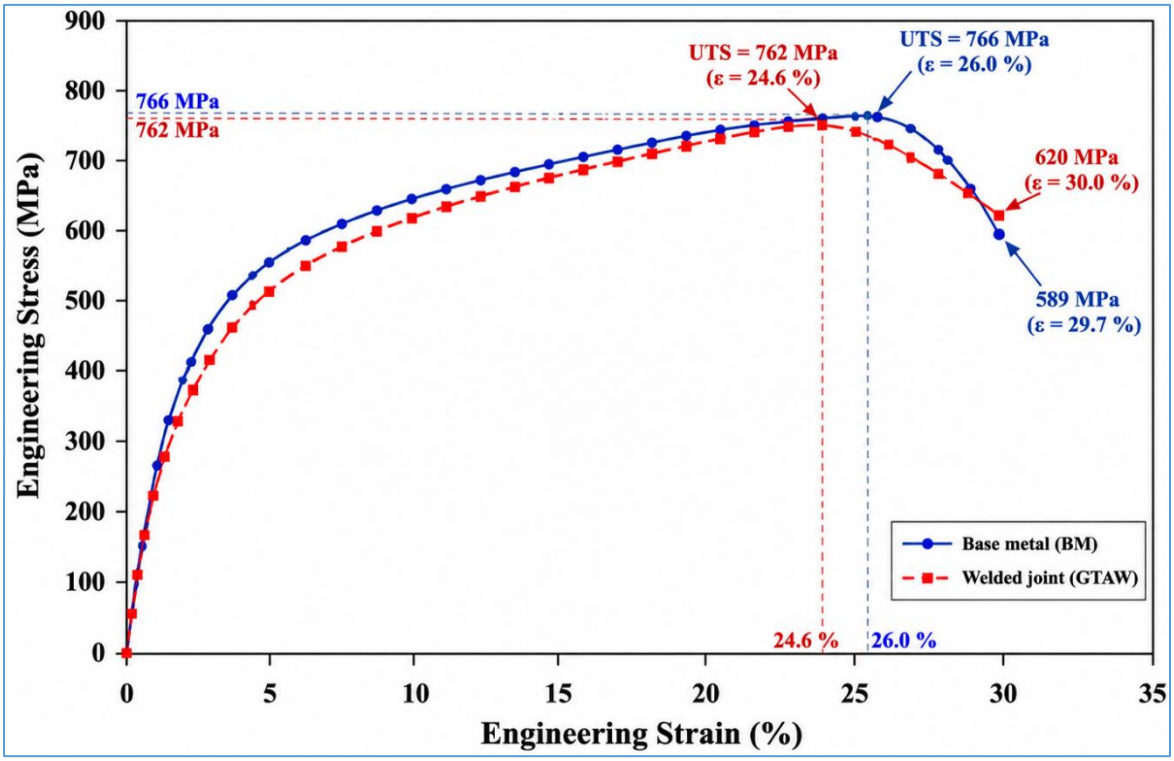

Figure 9: Stress-strain diagram for base metal and GTAW welded joint.

3.4 Effect of Chromium, Nickel and Molybdenum on the Mechanical Properties and Phase Balance of Duplex Stainless Steel 2205

Figures 10(a), 10(b), and **10(c)** present the impact of Cr, Ni, and Mo alloying elements on the mechanical properties and phase stability of DSS 2205 respectively. In the case of GTAW, these elements are instrumental in ferrite-austenite transformation, the solidification of weld metal, grain structure and hardness distribution as well as tensile behaviour. One must distinguish the influence of alloy composition from that of the welding thermal cycle. Since autogenous GTAW is performed without a filler metal, the chemical composition does not undergo any major alteration; it is the thermal cycle of the welding that causes the alloying elements to be redistributed between the ferrite and austenite phases. Chromium, acts as a ferrite stabilizer and is what provides oxidation resistance, a passive film and corrosion protection. In GTAW the weld pool will see ferrite solidify first on account of the phase's stability at elevated temperatures. Nickel by contrast is an element that stabilizes austenite. As the temperature drops, austenite will start to nucleate and grow at the ferrite grain boundary and within the grain itself. The chromium content has a bearing on this transformation because of its propensity to partition to the ferrite, so the ferritic phase in regions with a greater ferrite fraction will have more chromium. The data shows the ferrite fraction going from 20% to 70%

and the chromium from 16 to 27.5 wt. % while the austenite is reduced from 80% to 30%. If the cooling rate on a genuine GTAW joint is too high to permit sufficient reforming of austenite, there will be an over retention of ferrite which can have an impact on toughness and corrosion resistance. A good duplex structure requires adequate austenite formation on cooling. For that reason the UTS and hardness figures presented should be viewed as general compositional examples rather than a straight prediction of GTAW weld properties. With DSS 2205 the GTAW technique subjects the material to a thermal cycle that yields a ferrite-rich structure before austenite nucleation and growth set in during the cool down. The nickel in the austenite serves to stabilize it and determine the final ratio of ferrite to austenite. The figure below illustrates how an increase in nickel from 2 to 12 wt.% sees the austenite fraction rise from 25% to almost 88% and the ferrite fall from 75% to 10%. In practice the extent of austenite refounding is a function of the peak temperature, time for transformation, chemical makeup and the rate of cooling. Too rapid a cooling will produce an excess of ferrite at the expense of the austenite, while the right kind of cooling is conducive to a balanced duplex. Moreover the nickel enrichment is of assistance in preserving the ductility and toughness of the austenitic phase. The upper panel gives a schematic view of the UTS variation. Tensile strength is really a matter of the phase morphology, grain size, deformation in the two phases and any welding defects. Molybdenum is the agent for pitting and crevice corrosion and for ferrite stabilization. It is possible in the GTAW process for molybdenum to segregate to the ferrite in preference to the austenite and so alter the composition of the phases, as the elemental analysis of different regions would show, if only to varying degrees. From the phase fraction graph shown schematically below, there is a reduction in austenite from 80 to 60 % while there is an increase in ferrite from 20 to 40 % with molybdenum content increasing from 2 to 8 wt. %. There is also the likelihood of increased precipitation of intermetallic phases such as sigma and chi as a result of excess molybdenum and its retention for long periods within suitable temperature range in welded DSS 2205. Hardness and strength trends above should not be generalized as it is dependent on the microstructure developed.

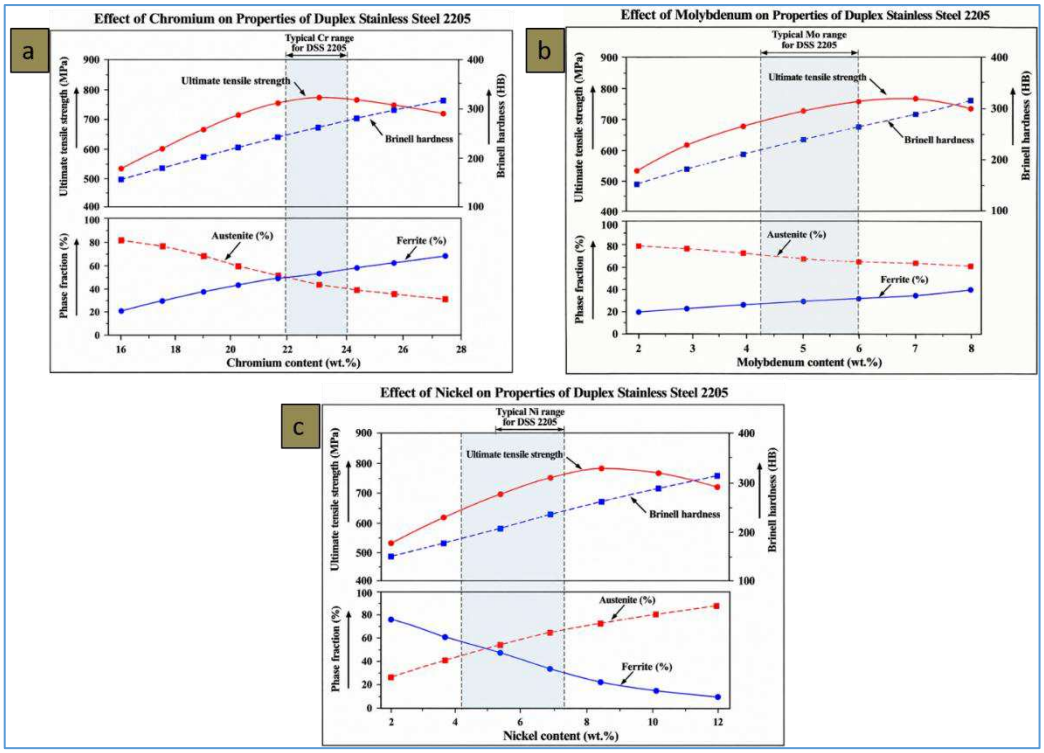

Figure 10: Effects of (a) chromium, (b) molybdenum and (c) nickel content on the mechanical properties and phase balance of welded DSS 2205.

3.5 Fractographic Analysis of the Tensile-Fractured DSS 2205 Welded Joint

Figure 11(a) represents the fractured tensile sample of DSS 2205 after mechanical testing. The red ellipse indicates the area where the sample fractured at its gauge section. An SEM analysis was carried out on the chosen fracture surface to determine the failure mechanism and morphology. The resulting fractograph of the Duplex Stainless Steel (DSS 2205) tensile sample, obtained at 10kV accelerating voltage with 500× magnification, is dominated by ductile fracture characteristics. In the region under examination the fracture surface is replete with microscopic dimples and microvoids. As **Figure 11(b)** demonstrates, these are evidence of failure through the nucleation, growth and coalescence of microvoids. The presence of a fine and close dimples points to extensive plastic deformation before the fracture. Such microdimples come about when microvoids nucleate at inclusions, precipitates or sites of microstructural discontinuity under tensile stress. Further deforming the material causes the voids to enlarge and coalesce into microdimples on the surface. Some variation in dimple size is apparent from the SEM fractograph, with both large cavities and finer ones on the fracture surface. The larger dimples may be taken as signs of localized plastic deformation and microvoid formation, whereas the smaller variety would suggest multiple void formation points. Irregular spots of bright contrast are visible in various places. While these could be

fractured or pulled out secondary phase particles, inclusions or some kind of deposit, their chemistry is not discernible from the secondary electron image. The lack of any extensive well-formed cleavage facets or river patterns would show that cleavage fracture did not play any major role in the failure of the material. The dimpled nature of the fracture surface shows that the welded sample of the DSS 2205 had undergone significant amount of plastic deformation prior to failure due to tensile stress. This is a confirmation of the ductile fracture of the material and is in line with the behavior of the material in the tensile test.

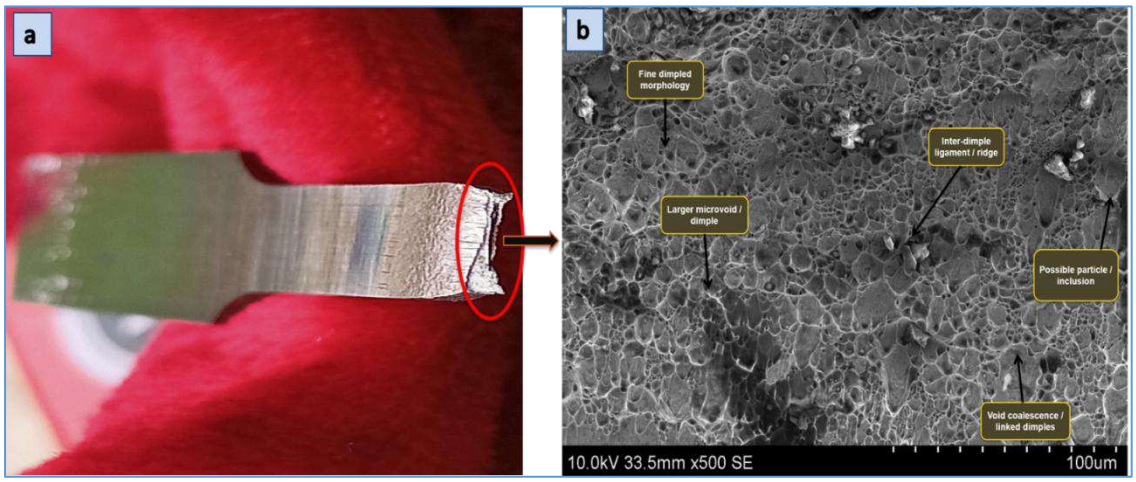

Figure 11: Tensile fracture appearance and SEM fractography (a) macroscopic view of the fractured tensile specimen, (b) SEM micrograph of the fractured surface.

3.6 Integrated Stress–Strain Response and Energy Absorption Characteristics

In order to assess the tensile behavior of DSS 2205 even further, the area beneath the engineering stress-strain curve for both samples is computed by integration numerically according to the trapezoidal rule. It gives the information about mechanical energy absorbed per unit volume in some specific strain range. Engineering strain values are transformed from percentage to a dimensionless form before integration; therefore, the area has the units of MPa or MJ m^{-3}. Two integration ranges are used first from the start of loading to the strain at the UTS, and second over the whole available strain range from the data. Base metal had an integral value of the stress-strain curve of 141.13 MJ m^{-3} till UTS, whereas GTAW welded joint had 122.44 MJ m^{-3} over the same strain range. Welded specimen has a lower integral value by 13.24% till UTS, although it has 99.48% of UTS of base metal. The strain of the UTS reduced from 26.0% for the base metal to 24.6% for the welded joint, which represents a reduction of 1.4% or 5.38% compared to the base metal. If the integration period extends through the total range of the data, the areas will be 168.12 MJ m^{-3} for the base metal and 162.37 MJ m^{-3} for the

welded joint shown in **Figure 12**. The difference reduces to 3.42%. To be precise, the base metal's graphs end at 29.7% strain and 589 MPa, as against 30.0% strain and 620 MPa for the welded joint. One can view the integrated area to UTS as a way of comparing the response in terms of energy absorption prior to peak load. The whole of the curve plotted in the course of the test is merely the cumulative area in the test range. Neither should be put down as the actual fracture toughness or total energy to failure unless it is verified that the specimen went to complete separation. The weld joint has kept its peak strength in line with the base material, though the integrated value is a touch lower. This is due to the little lower strain at UTS in the welded joint. The tensile tests show the base metal hitting a maximum UTS of 766 MPa at 26.0% strain. The welded joint comes in at 762 MPa at around 24.6% strain. That is a 4 MPa, or 0.52%, drop relative to the base metal, meaning the joint has 99.48% of the base metal's tensile strength. The GTAW parameters have produced a joint capable of taking tensile loads much like the parent metal. Whether this small variation is of statistical significance remains to be seen in further testing. Looking at the experimental stress-strain curves, engineering stress rises with strain before plastic deformation and strain-hardening set in. The base metal puts up higher stress in places during the plastic phase but the welded metal does the same at higher strains. The two specimens reach their maximums in the same ballpark. At peak stress the curves for both go down in engineering stress in keeping with necking and localised deformations. The welded joint gets to its maximum at a little less strain than the base material so there is a divergence in the way it deforms. But from the data at hand the exact figure for fracture strain or any loss of ductility cannot be ascertained. Numerical von Mises stress contours, presented in **Figure 13(a)** and **13(b)**, present the stress distribution in the base-metal specimen during tensile test. The legend of the von Mises stress contours shows that the maximum value of von Mises stress is about 277.1 MPa. The non-uniformity of stress distribution is visible for the given specimen, as the reduced gauge region and its vicinity to the transition zone have relatively high stress concentration. The green and cyan contours correspond to intermediate values of stress, whereas blue areas demonstrate relatively low values of the equivalent stress. This variation in stress is influenced by the geometry of the specimen and its deformation under loading conditions. **Figure 13 (c)** and **13 (d)** illustrates the von Mises stress contour plot for the GTAW-welded specimen. The contour image displays a maximum von Mises stress of some 264.8 MPa that is less than the contour maximum for the base-metal specimen. Stress is high in zones along the reduced section and in the centre of the specimen other areas are not as highly stressed. A change in local stress distribution can be expected where the welded joint gives way to the adjoining material on account of

microstructural differences between the weld, HAZ and base metal. The numerical values of the contour maxima, the welded specimen has a maximum von Mises stress 4.4% below that of the base-metal specimen. This difference is what is seen in the finite element models at the stages of simulation shown. It should not be taken as a reduction in tensile strength since the contour maxima are dependent on displacement, loading rate, boundary conditions, the strain state and material properties. The numerically computed maximums of 277.1 and 264.8 MPa are well below the UTS of 766 and 762 MPa determined by experiment given in Table 5. The present contours therefore give a qualitative picture of the stress distribution, not a quantification of the experimental tensile strength. One can also draw a correlation with the SEM fractography of the tensile fractured weld sample. The fine and large dimples, micro voids and inter-dimples ligaments point to a ductile fracture involving the nucleation, growth and coalescence of microvoids. The finite element model's prediction of local stress concentration may correspond to areas of greater deformation, though the location of the fracture area as initiated in the experiment would have to be confirmed. As per numerical studies, the DSS 2205 GTAW welded joint maintains its tensile strength at virtually the same level as the base material, with the UTS held at about 99.48%. The Abaqus simulation results shed light on the unevenness of the stress distribution and the local concentrations in both samples. **Figure 14(a)** compares the FE and experimental outcomes while **Figure 14(b)** presents the normalised retention of the tensile and numerical parameters. For the finite element analysis to be a proper numerical validation, the material parameters ascertained in the experiments must be used, together with consistent units, the right boundary conditions and a convergence study of the mesh and reaction forces versus displacement output.

Table 5: Integrated engineering stress–strain area for DSS 2205 base metal and GTAW-welded joint.

Parameter	Base metal	GTAW welded joint	Difference
UTS (MPa)	766	762	4 MPa lower in welded joint
Strain at UTS (%)	26.0	24.6	1.4 % points lower
Area up to UTS (MJ m^{-3})	141.13	122.44	13.24% lower
Area over complete recorded range (MJ m^{-3})	168.12	162.37	3.42% lower
Last recorded strain (%)	29.7	30.0	0.3 % points higher in welded joint
Last recorded stress (MPa)	589	620	31 MPa higher in welded joint

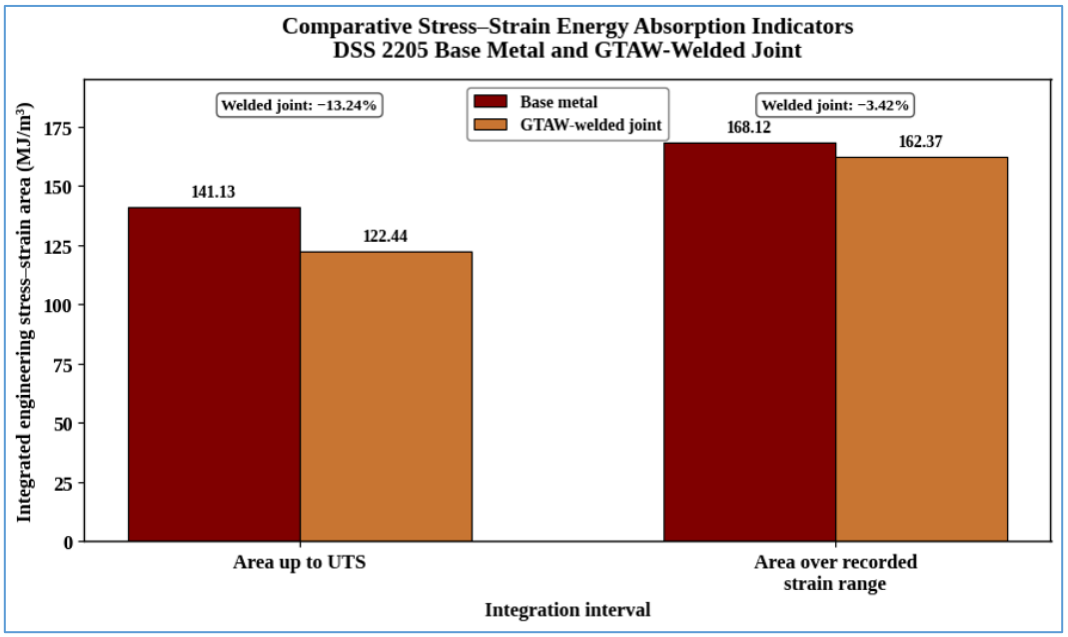

Figure 12: Finite Element Analysis and Experimental Validation of Tensile Behaviour of DSS 2205 Base Metal and GTAW-Welded Joint.

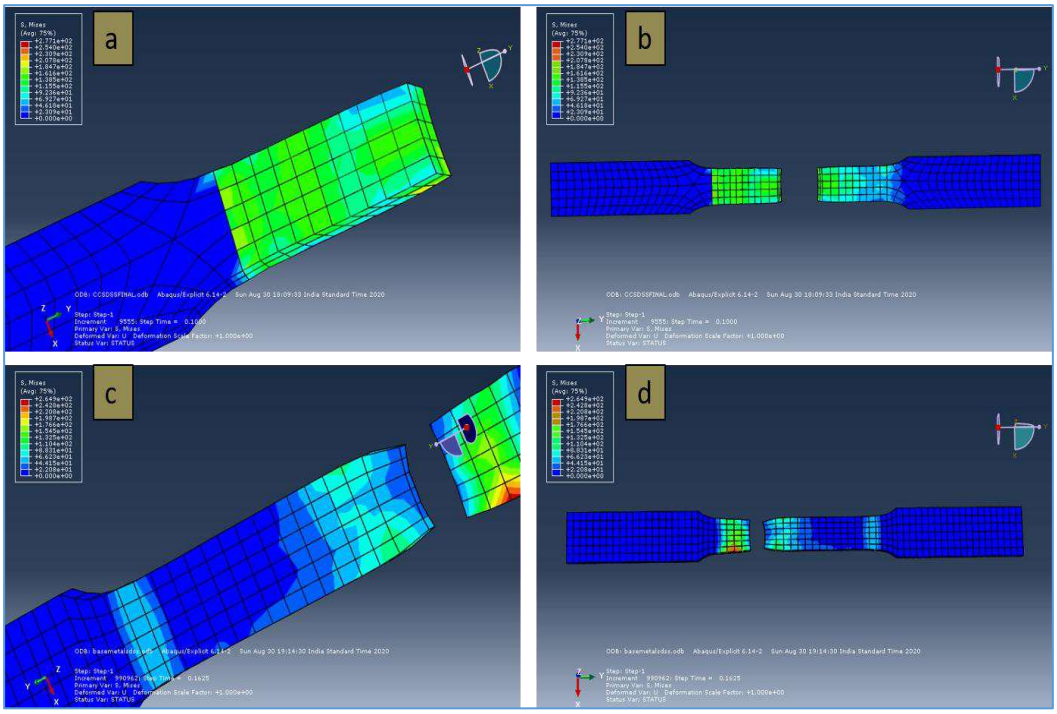

Figure 13: Stress-Strain Energy Absorption for base metal and welded joint.

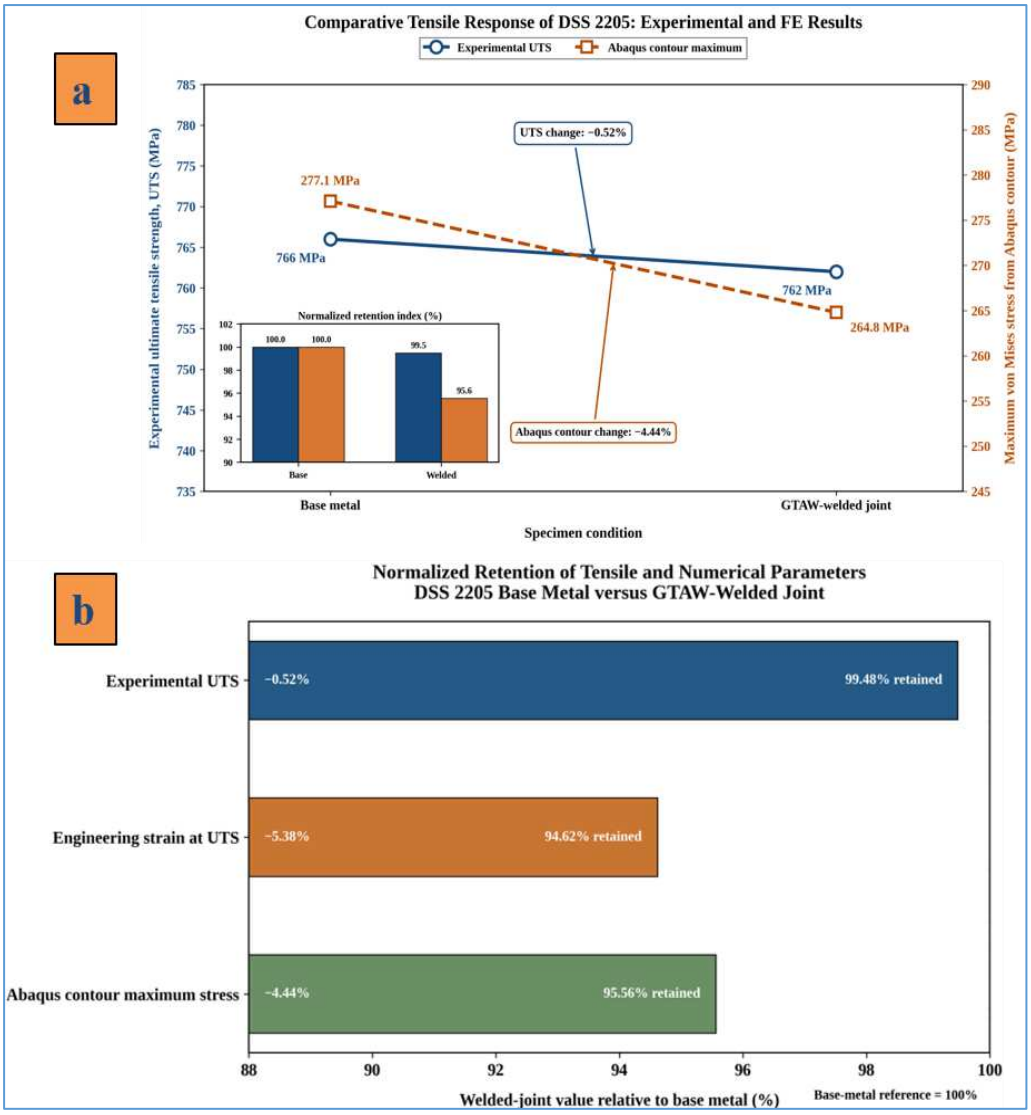

Figure 14: Tensile strength analysis (a) comparison of experimental and FE results, and (b) normalized retention of tensile and numerical parameters.

Conclusion

This study investigated the microstructure, mechanical properties and fracture behavior of DSS 2205 stainless steel plates that are welded by using autogenous Gas Tungsten Arc Welding (GTAW) process. Parameters used in welding, which include 80 A current, 12 V voltage and travel speed of 100 mm/min and 15 L/min argon shielding gas, led to the fabrication of sound welds. The average electrical energy input per unit length is 0.576 kJ/mm. Phase analyses gave the ferrite content in the base material, HAZ and WZ of 48.4%, 50.2% and 51.7% respectively. Austenite contents are 51.6%, 49.8% and 48.3% in base material, HAZ and WZ respectively. It is evident that there is gradual increase in ferrite content from base material up to the fusion zone. Composition analysis by using SEM–EDS shows composition separation between the two phases, mainly the partitioning of nickel into austenite, in agreement with the fact that

nickel stabilizes the austenitic structure. Average microhardness values are found to be 221.25 HV, 231.67 HV and 239 HV in the base metal, HAZ and fusion zone respectively. As per the tensile test, both the base metal and weld joint are able to have tensile strengths of 766 MPa and 762 MPa respectively, representing tensile strength retention of 99.48%. The value of strain at UTS is reduced from 26.0% to 24.6%. The SEM fractography showed mainly ductile type of failure characteristics such as fine and large dimples, micro voids and inter-dimple ligaments. The combined stress-strain analysis showed a 13.24% decrease in the area up to UTS and 3.42% overall area in the total recorded values. The maximum von Mises stresses of base metal and welded specimens from the Abaqus simulation are 277.1 MPa and 264.8 MPa respectively. In general, the results show that the GTAW technique used provided tensile strength comparable to the base metal.

Declaration

Ethical Approval: This article contains no studies with human participants or animals performed by the author. The author used benchmark datasets or publicly available datasets.

Consent for publication: Not applicable.

Competing interests: The authors declare no competing interests.

Authors' contribution: S.J.: Conceptualization, methodology, formal analysis, investigation, visualization, writing – original draft, and project administration. A.L., S.M.: Supervision, validation, methodology, interpretation of results, critical review and editing of the manuscript, and final approval of the submitted version. All authors have read and approved the final manuscript.

Funding Information: The authors received no funding from their institutes for this research.

Data availability: Data will be available on request.

References

[1] Z. Fei, Z. Pan, D. Cuiuri, H. Li, S. Van Duin, Z. Yu, Microstructural characterization and mechanical properties of K-TIG welded SAF2205/AISI316L dissimilar joint, Journal of Manufacturing Processes 45 (2019) 340-355.

[2] C. Shravan, N. Radhika, N. Deepak Kumar, B. Sivasailam, A review on welding techniques: properties, characterisations and engineering applications, Adv. Mater. Process. Technol 10(2) (2023) 1126-1181.
[3] C. Köse, H.B. Mutu, F. Doğan, Effect of post weld heat treatment and filler wire on mechanical properties and microstructure of tungsten inert gas welded AISI 2507 super duplex stainless steel, Journal of Materials Engineering and Performance 34(19) (2025) 22340-22354.
[4] M. Zhang, J. Ma, J. Huang, X. Luo, F. Yin, F. Guo, X. Wang, J. Yi, Evaluation microstructure and corrosion behavior of different keyhole TIG welded joints of duplex stainless steel grade 2205 pipe, International Journal of Pressure Vessels and Piping 215 (2025) 105459.
[5] Q. Chu, D. Yang, Z. Chang, K. Cao, W. Xie, G. Liu, F. Yan, Investigation on microstructure evolution, mechanical properties and corrosion resistance of dual phase stainless steel joints welded by GTAW and SAW methods, International Journal of Pressure Vessels and Piping 209 (2024) 105183.
[6] R. Kumar, A.P. Agrawal, M. Maurya, S. Ali, M.K. Giri, A. Kumar, N.K. Maurya, Influence of Heat Input on Phase Balance, Microstructural Evolution, and Mechanical Performance of Super Duplex Stainless Steel Welded by Gas Tungsten Arc Welding, Journal of Materials Engineering and Performance (2026) 1-8.
[7] M.H. Sar, S.H. Shahatha, S. Chatti, M. Zidi, Influence of Interpass Welding Temperature on the Microstructure and Mechanical Properties of Super Duplex Stainless Steel AISI 2507, Diyala Journal of Engineering Sciences (2026) 171-180.
[8] S. Onifade, O. Sogunro, V. Ogundemuren, Comparative Evaluation of Shielded Metal Arc Welding and Gas Tungsten Arc Welding on Stainless Steel Joints, International Journal of Women in Technical Education and Employment 7(1) (2026) 47-60.
[9] S. Manivannan, M. Karthikeyan, C.R. Kannan, B. Srinivasan, A.D. Das, V. Santhosh, Effect of different filler materials on the performance of Gas Tungsten Inert Gas welded joints of HSLA 950C and DSS 2205, AIP Conference Proceedings, AIP Publishing LLC, 2026, p. 020035.
[10] M.R. Maulana, E.W.R. Widodo, Pengaruh Variasi Konsentrasi Hidrogen Fluorida dan Temperatur Proses Pickling terhadap Ketebalan Lapisan Oksida serta Pitting Corrosion pada Sambungan Las Gtaw Stainless Steel 304l, Integrative Perspectives of Social and Science Journal 3(08 Agustus) (2026) 1045-1057.
[11] A. Khaled, M. Djendel, A. Kellai, A. Astarita, W. Jomaa, Effect of PWHT on microstructural evolution, mechanical properties, and corrosion behavior of GTAW-welded

AISI 316 stainless steel, The International Journal of Advanced Manufacturing Technology (2026) 1-18.
[12] M. Sohel, V.S. Sharma, A. Arumugam, Fusion welding processes parameter optimization for critical piping systems: A comprehensive review, Journal of Manufacturing and Materials Processing 10(1) (2026) 40.
[13] A. Garga, S. Sirohi, D. Fydrych, C. Pandey, Role of the buttering layer in microstructural and mechanical characteristics of dissimilar IN617-AISI 304 H welded joints fabricated by multi-pass GTAW, The International Journal of Advanced Manufacturing Technology 144(7) (2026) 5493-5523.
[14] F.K. Nugroho, M.A.F. Hendrawan, Studi Pengaruh Polaritas Arus Pengelasan SMAW dan GTAW Pada Lembaran Stainless Steel Metode Pengujian Impact: Study of the Effect of SMAW and GTAW Welding Current Polarity on Stainless Steel Sheets Impact Testing Method, Jurnal Pendidikan Teknik Mesin Undiksha 14(2) (2026) 133-145.
[15] H. Li, J. Che, T. Cai, Research on Stress Evolution and Low-Stress Recrystallized Microstructure Control in TIG Welding of 7075 Aluminum Alloy Based on Thermomechanical Coupling, Journal of Materials Engineering and Performance (2026) 1-15.
[16] M. Sahu, A. Ghosh, A. Das, M. Ghosh, S.P. Sagar, Impact of wire feed rate on mechanical properties of GMA Welded joints: a qualitative evaluation using nonlinear ultrasonic technique, Nondestructive Testing and Evaluation 41(9) (2026) 5430-5457.
[17] S. Petla, R.S. Vidyarthy, Metallurgical and mechanical properties evaluation of the activated flux tungsten inert gas weldments, Proceedings of the Institution of Mechanical Engineers, Part E: Journal of Process Mechanical Engineering 240(1) (2026) 1161-1182.
[18] H. Xu, Y. Zhang, L. Han, J. Lv, R.N. Bakhtizin, Analysis of Microstructure and Mechanical Properties of Keyhole Gas Tungsten Arc Weld Metal in 9% Ni Steel, Journal of Materials Engineering and Performance (2026) 1-10.
[19] P. Kanagaraj, B. Visvalingam, V. Varadhan, K. Radhakrishnan, Influence of root pass welding techniques (GTAW and RMD) on metallurgical, mechanical and corrosion behaviour of gas metal arc welded duplex stainless-steel plates, Canadian Metallurgical Quarterly (2026) 1-27.
[20] A. Sharma, S. Gudikandula, B.R. Sunil, A. Kumar, Morphological characterisation, tribological behaviour and corrosion resistance of GTAW and SMAW welded lean duplex stainless steel S32101, Canadian Metallurgical Quarterly (2026) 1-15.
[21] J. Wang, Z. Sun, C. Yu, W. Zheng, R. Zong, Study on the mechanism of laser-arc hybrid welding in improving the weld quality of 2507 super duplex stainless steel, (2026).

[22] R. Boz, Z. Taşlıçukur Öztürk, D. Gürkan, TIG Welding of EN 1.3964 Low-Magnetic Austenitic Stainless Steel: Effects of Welding Parameters on Microstructure, Mechanical Behavior, and Ferrite Stability, Materials Research Express (2026).
[23] A. Ebrahimpour, P. Alipour, T. Saeid, Microstructural analysis and finite element simulation of hybrid GTAW–GMAW welding on AISI 316 L stainless steel, The International Journal of Advanced Manufacturing Technology (2026) 1-19.
[24] P.N. Bellamkonda, L. Gudapati, M. Dwivedy, R. Addanki, B. Visvalingam, A. Thirugnanasambandam, V. Kalluri, Comparative study on metallurgical, mechanical and corrosion behaviour of dissimilar Inconel 718 and AISI 410 welds using constant current and pulsed current gas tungsten Arc welding processes, Canadian Metallurgical Quarterly 65(2) (2026) 1769-1788.
[25] S. Kumar, K. Vimal, Numerical and experimental studies of thin super duplex stainless steel GTAW joints, International Journal of Materials Engineering Innovation 15(2) (2024) 157-171.
[26] M.A. Makhdoom, A. Ahmad, M. Kamran, K. Abid, W. Haider, Microstructural and electrochemical behavior of 2205 duplex stainless steel weldments, Surfaces and Interfaces 9 (2017) 189-195.
[27] R. Mohammed, G. Madhusudhan Reddy, K. Srinivasa Rao, Effect of welding process on microstructure, mechanical and pitting corrosion behaviour of 2205 duplex stainless steel welds, IOP Conference Series: Materials Science and Engineering, IOP Publishing, 2018, p. 012026.
[28] B.E. Çelik, Ş. Talaş, Mechanical properties of UNS S31803 (2205) duplex SS welds deposited with GTAW and SMAW methods, Soldagem & Inspeção 29 (2024) e2913.
[29] K. Touileb, A.C. Hedhibi, R. Djoudjou, A. Ouis, A. Bensalama, A. Ibrahim, H.S. Abdo, M.M.Z. Ahmed, Mechanical, Microstructure, and Corrosion Characterization of Dissimilar Austenitic 316L and Duplex 2205 Stainless-Steel ATIG Welded Joints, Materials 15(7) (2022) 2470.
[30] S. Gao, S. Geng, P. Jiang, G. Mi, C. Han, L. Ren, Numerical analysis of the deformation behavior of 2205 duplex stainless steel TIG weld joint based on the microstructure and micro-mechanical properties, Materials Science and Engineering: A 815 (2021) 141303.
[31] J. Verma, R.V. Taiwade, Effect of welding processes and conditions on the microstructure, mechanical properties and corrosion resistance of duplex stainless steel weldments—A review, Journal of Manufacturing Processes 25 (2017) 134-152.